

Absolute differential cross sections for the excitation of molecular oxygen by electron impact: Decomposition of the Schumann-Runge continuum

Tong W. Shyn, Christopher J. Sweeney, Alan Grafe, and William E. Sharp

Space Physics Research Laboratory, University of Michigan, Ann Arbor, Michigan 48109-2143

(Received 18 July 1994)

Using a crossed-beam method, we have measured electron-energy-loss spectra for the excitation of the Schumann-Runge continuum of molecular oxygen. The scattering angle and electron-impact energy ranges covered were 12° – 156° and 15–50 eV, respectively. By means of computerized least-squares analysis, we decomposed the spectra into contributions from three superposed Gaussian line shapes. The two lowest in energy are identified as representing excitation of the $1^3\Pi_g(v)$ and $B^3\Sigma_u^-(v)$ states. The other line shape cannot be definitively identified, but we discuss several possibilities for its meaning. Absolute differential and integrated cross sections for all three states are obtained, along with linear electronic potential-energy curves for the Franck-Condon region.

PACS number(s): 34.80.Gs

I. INTRODUCTION

The very important role of molecular oxygen's Schumann-Runge (SR) continuum in filtering solar ultraviolet radiation has been known for many years [1]. Besides providing the bulk of the atmospheric opacity in the 1400–1700-Å spectral region, excitation of the SR continuum results in the production of oxygen atoms in both their ground and excited states, the mixture of these depending on the excitation mechanism involved [2]. This mixture is crucial in determining the progress of atmospheric chemical reactions. The SR continuum is also known to arise from several overlapping electronic states, some of which are believed to be strongly perturbed and not electric dipole connected to O_2 's ground electronic $X^3\Sigma_g^-$ state. The SR continuum's nature is therefore important in environmental science as well as being important in basic chemistry and physics.

The first quantitative photoabsorption experiments on the SR continuum were performed by Ladenburg and Van Voorhis more than half a century ago [3]. Since then, numerous additional optical measurements have been performed. (See, for instance, the reviews by Hudson [4] and Krupenie [5].) As a result of this extensive research, our knowledge of the opacity and photoabsorption data on the SR continuum is now fairly complete. Additionally, Lee *et al.* [6] measured the quantum yield of ground- and excited-state oxygen atoms produced as a result of the optical excitation of the SR continuum. They determined that the atoms were produced in their ground (3P) and first excited state (1D) in equal amounts, presumably from the excitation of the electric dipole accessible $B^3\Sigma_u^-(v)$ state. No atoms in their second excited (1S) state were observed, however.

In addition to the extensive optical research, there have also been many theoretical treatments of the electronic states of O_2 that comprise the SR continuum, and all these treatments indicate that the situation is quite complex. (See, for instance, Refs. [7–13].) While, quan-

titatively, the results of these studies frequently disagree, qualitatively they all indicate substantial valence-Rydberg perturbations among many of the states and also transition moments to the repulsive states which are often nonconstant in the Franck-Condon (FC) region.

Unlike the case of optical measurements and theoretical calculations, however, very little research has been done on the low-energy electron-impact excitation of the SR continuum. As indicated in the reviews by Trajmar, Register, and Chutjian [14], Trajmar and Cartwright [15], and Itikawa *et al.* [16], the data here can be characterized as fragmentary at best, with large gaps in both the impact energy and scattering angle ranges. The only comprehensive set of measurements was performed by Wakiya [17,18]. He used an energy resolution of about 200 meV to measure electron energy-loss spectra for the SR continuum over the impact-energy range 20–500 eV and the scattering angle range 5° – 130° . He obtained excitation cross sections, but did not decompose the spectra into contributions from the various states involved.

This is unfortunate because in addition to being an important process in the upper atmosphere, low-energy electron-impact excitation does not obey the stringent optical selection rules and thus allows significant population of optically forbidden states. For example, using electron-impact excitation, Trajmar, Cartwright, and Hall [19] and York and Comer [20] observed vibrational excitation of the optically inaccessible $C^3\Pi_g(R)$ and $d^1\Pi_g(R)$ states as discrete structures superposed on the strong valence state portion of the SR continuum. Recently, Sur *et al.* [21,22] detected Rydberg states of the same symmetry by a two-photon and subsequent ionization technique. The triplet state they observed was the same as that seen in the electron-impact experiments. The singlet state was not the same, though they made a definite assignment and performed a rotational analysis. These data all support the notion of strong valence-Rydberg perturbations indicated by the theoretical studies.

To date, there has been only one attempt to unfold the SR continuum produced by low-energy electron impact into contributions from its constituent states. Cartwright *et al.* [23] decomposed twelve such spectra into both valence and Rydberg contributions. In addition to the low-energy spectra, they also analyzed a 25-keV, 0° scattering angle spectrum provided to them by Geiger and Schröder [24]. The latter high-energy spectrum is equivalent in structure to photoabsorption spectra. Cartwright *et al.* determined that the Rydberg contributions to this high-energy spectrum were minor, and that the primary contribution came from the $B^3\Sigma_u^-(v)$ state. In addition, they found substantial contributions from the $1^3\Pi_u(v)$ and $1^3\Pi_g(v)$ states, both of whose excitation results in the dissociation of O_2 via the $O(^3P)+O(^3P)$ channel. The former state's excitation is optically allowed, but is predicted to provide very small contributions [9]. Excitation of the latter state occurs through the magnetic dipole interaction and thus should also be weak. While the results of Lee *et al.* contradict these findings for high-energy electron-impact spectra, they do not preclude the presence of optically forbidden states in low-energy electron-impact spectra.

In this paper, we present the results of the first extensive decomposition of low-energy SR electron-impact spectra. A total of 338 spectra were measured, covering the scattering angle and impact-energy ranges of 12° – 156° and 15–50 eV, respectively. The data were analyzed by means of a computerized least-squares technique. A model based on the assumptions of linear potential-energy curves in the FC region and constant transition moments was employed, as accurate corrections to these assumptions are not yet available. Three valence contributions were determined ($1^3\Pi_g(v)$, $B^3\Sigma_u^-(v)$, and one unidentified). Rydberg contributions were found to be only minor in this energy range and thus were neglected. In addition to yielding the forms of the potential-energy curves, the model also provided absolute differential (DCS) and integrated (ICS) cross sections.

II. EXPERIMENT

The apparatus and procedures we employed for our Schumann-Runge measurements were essentially the same as those we utilized for our previous electron- O_2 scattering experiments [25–29] and are given detailed accounts elsewhere in the physics literature [30–32]. We thus provide only a rudimentary description here. Comprising our apparatus are three principal subsystems: a neutral-molecular-oxygen-beam source, a monoenergetic electron-beam source, and a scattered-electron detector. All three subsystems are housed in a high-vacuum enclosure, which is divided into differentially pumped upper and lower chambers. Three orthogonal sets of Helmholtz coils surround the vacuum enclosure to reduce stray magnetic fields, including the magnetic field of the Earth, to less than 20 mG in all directions in the interaction region. The energy scale of our measuring apparatus was calibrated via the 19.35-eV resonance of helium.

The neutral-molecular-oxygen-beam source resides in

the upper chamber. Research-grade O_2 is piped into this chamber from a commercial storage cylinder. The piping terminates at a capillary array positioned at the interface between the two chambers. A vertically collimated molecular beam is thus provided in the lower chamber, where the electron-molecule collisions occur.

The electron-beam source is mounted on a turntable in the lower chamber and can be rotated from -90° to $+160^\circ$ in a continuous fashion. Comprising the beam source are an electron gun with a thoriated-iridium filament, a 127° cylindrical energy selector, two electron lens systems, and two beam deflectors. Currents in excess of 10^{-8} A are produced by this subsystem, while the angular divergence of the electron beam is approximately $\pm 3^\circ$.

Also residing in the lower chamber is our scattered-electron detector. The detector is made of a 127° cylindrical and a hemispherical energy analyzer in series, two electron lens systems, and a Channeltron electron multiplier. This arrangement provides a signal-to-noise ratio more than 100 times better than the single analyzer system we have employed in the past.

We know from our previous experiments that the line shape that characterizes our overall machine response (i.e., the energy profile of the electron beam convolved with the detector's response function) is well represented as Gaussian in energy and for the present set of measurements was fixed at about 80 meV full width at half maximum (FWHM). Note that such an energy resolution allows us to resolve vibrational and nonoverlapping electronic excitations but not rotational excitations.

During actual measurements the impact energy and scattering angle are fixed, while a dedicated microcomputer sweeps the energy acceptance window of the detector over the region of interest and also accumulates the data. We repeat our measurement process over the prescribed impact energy and angular ranges.

III. DATA ANALYSIS

We extracted differential cross sections and potential-energy curves in the FC region from our data by computerized least-squares analysis. The analysis was performed on Hewlett-Packard series 9000 workstations, a Cray YM-P/832 Supercomputer, and a Cray C90 Supercomputer. The FORTRAN90 computing language was employed. The details of the analysis process are as follows.

A. Form of the model spectra

For the case of ideal experimental conditions, i.e., if the machine response were a Dirac δ function in energy and there were no background noise, our energy-loss spectra would assume the form

$$s(\rho, S_0, \theta, E_i, E_l) = \rho S_0 G(\theta) \epsilon(E_i - E_l) \sum_{j=1}^N f_j(E_i - E_l) I_j(\theta, E_i). \quad (1)$$

Here, $s(\rho, S_0, \theta, E_i, E_l)$ is the scattered-electron signal strength, E_i the impact energy, and E_l the energy loss. ρ is the molecular beam density, S_0 the signal strength of

the incident electron beam, and θ the scattering angle. $G(\theta)$ and $\varepsilon(E_i - E_l)$ are functions characterizing the scattering geometry and detection efficiency, respectively. For the N states that are excited, the $f_j(E_i - E_l)$ are normalized natural excitation line shapes, while the $I_j(\theta, E_i)$ are the intensities of these line shapes.

As discussed previously, our machine response is not ideal and thus broadens the natural line shapes. We have employed Gaussians to describe the natural line shapes. We will justify this choice and indicate its limitations later. The convolution integrals that relate the natural and measured line shapes can be performed analytically, and the measured line shapes turn out to be Gaussian in form also. The degree of broadening of these measured line shapes is given by a convenient “triangle” equality;

$$\Delta_{\text{meas}} = \sqrt{\Delta_{\text{nat}}^2 + \Delta_{\text{MR}}^2}, \quad (2)$$

where Δ_{meas} , Δ_{nat} , and Δ_{MR} are the energy FWHM of the measured, natural, and machine-response line shapes, respectively. It is apparent from Eq. (2) that when the natural and machine-response widths differ substantially, the measured width can be approximated by the larger of the two. In our model spectra, we replace the natural line shapes $f_j(E_i - E_l)$ with broadened line shapes $F_j(E_i - E_l)$ when analyzing data and use Eq. (2) to extract Δ_{nat} .

We must also account for the noise background present in our measurements. We accomplish this by adding a term $B(E_i - E_l)$ to the model ideal spectra of Eq. (1). We chose a quadratic form for $B(E_i - E_l)$; in practice, the quadratic term is almost always eliminated by the computer fitting process, leaving only a linear contribution. We thus believe no higher-order terms to be necessary to describe the background noise adequately.

The model spectra we fit to our measured data thus have the form

$$\begin{aligned} s(\rho, S_0, \theta, E_i, E_l) \\ = \rho S_0 G(\theta) \varepsilon(E_i - E_l) \sum_{j=1}^N F_j(E_i - E_l) I_j(\theta, E_i) \\ + B(E_i - E_l). \end{aligned} \quad (3)$$

B. Least-squares minimization algorithm

We have tested several least-squares minimization algorithms for the purpose of determining best-fit model parameters, including steepest-descent methods [33], neural network methods [34], and the downhill-simplex-simulated-annealing method [35]. Of these three algorithms, we employed the downhill-simplex-simulated-annealing method for our analysis of the data presented in this paper. While the algorithm is not the most efficient of the three, it was the only one that consistently found the global minimum among the many possible local minima when presented with test data. Actual computer implementation was based heavily on the source code provided by Press and Teukolsky [35].

C. Determination of the cross sections

We employ known functional forms for $G(\theta)$ and $\varepsilon(E_i - E_l)$ and dispense with the constant factors ρ and S_0 . Thus the only parameters determined by the fitting process are the energy FWHM Δ_j and mean excitation energies V_{0j} of the measured Gaussian line shapes $F_j(E_i - E_l)$, the corresponding intensity factors I_j , and the noise background contribution. As the j th cross section is proportional to the area under the curve $I_j F_j(E_i - E_l)$, we may compute absolute inelastic differential cross sections by comparing inelastic and elastic areas and normalizing the known values of the elastic cross sections [25]. We thus have

$$\left[\frac{d\sigma}{d\Omega} \right]_{\text{inel}} = \frac{I_{\text{inel}} \Delta_{\text{inel}}}{I_{\text{elas}} \Delta_{\text{elas}}} \left[\frac{d\sigma}{d\Omega} \right]_{\text{elas}}. \quad (4)$$

After finding the differential cross sections, we numerically integrate them to generate integrated cross sections. To accomplish this we use the trapezoidal integration rule. This requires that we extrapolate our differential cross sections to both 0° and 180° , which we perform in a semiexponential fashion. For cases when the differential cross sections are strongly peaked in the forward direction, special attention is needed for the low-angle extrapolations; here we extrapolate in 3° increments below 12° , and interpolate in 3° increments between 12° and 24° . Due to the smallness of the factor $\sin\theta$ at these angles, this introduces an uncertainty of no more than 3% into our integrated cross sections. Such an uncertainty is negligible when compared to the uncertainty present in the measured differential cross sections. Any required interpolations were accomplished semiexponentially. The small number of these interpolations makes the uncertainty that they may contribute to the integrated cross sections negligible.

D. Determination of potential-energy curves

To determine the repulsive potential-energy curves for the valence states whose presence we detected in the SR continuum, we employed the notions on electronic transitions in molecules developed by Franck [36] and Condon [37,38]. We assumed the potential-energy curves are linear in the Franck-Condon region and that the transition probability between the ground state and the valence state in question are constant with respect to the internuclear distance R . “Reflecting” the Gaussian ground-state nuclear-vibrational probability density from the linear FC region potential-energy curve,

$$V(R) = \gamma(R - R_0) + V_0, \quad (5)$$

we obtain a Gaussian excitation line shape. Here, R_0 is the equilibrium internuclear distance in the ground state, which is 1.208 Å for O_2 . The value of the slope γ in Eq. (5) is directly seen to be the ratio of the FWHM of the natural excitation line shape to that of the ground-state probability density. The latter quantity is 0.08599 Å for O_2 . The value of V_0 in Eq. (5) is simply the mean vertical excitation energy of the Gaussian excitation line shape.

TABLE I. Percentage uncertainty in measurements.

State	$1^3\Pi_g(v)$	$B^3\Sigma_u^-(v)$	Unknown
Source of uncertainty			
Statistical	3	3	3
Line shape	15	5	12
Detector efficiency	10	10	10
Elastic cross section	14	14	14
Total	23	18	21

E. Propagation of uncertainty

There are several sources of uncertainty that affect our analysis. The statistical uncertainty in the raw data is less than $\pm 3\%$. Consideration of the covariance matrices associated with the fits in the line shape yields formal uncertainties for the values of I and of Δ for each state in Eq. (4). For the $1^3\Pi_g(v)$ state, the uncertainty in I is $\pm 8\%$ and in Δ is $\pm 12\%$. For the $B^3\Sigma_u^-(v)$ state, the uncertainty in I is $\pm 2\%$ and in Δ is $\pm 3\%$. For the unknown state, the uncertainty in I is $\pm 10\%$ and in Δ is $\pm 5\%$. The uncertainty in the detector efficiency correction is $\pm 10\%$, and uncertainty in the elastic cross sections used for normalization of the present results is $\pm 14\%$. The uncertainties in the DCS's for the $1^3\Pi_g(v)$, $B^3\Sigma_u^-(v)$, and the unknown states therefore become $\pm 23\%$, $\pm 18\%$, and $\pm 21\%$, respectively. These results are summarized in Table I. For the ICS's, an additional uncertainty of less than $\pm 3\%$ is introduced by the extrapolation and interpolation of the DCS's. The overall uncertainty in the ICS's is therefore comparable to that in the corresponding DCS's.

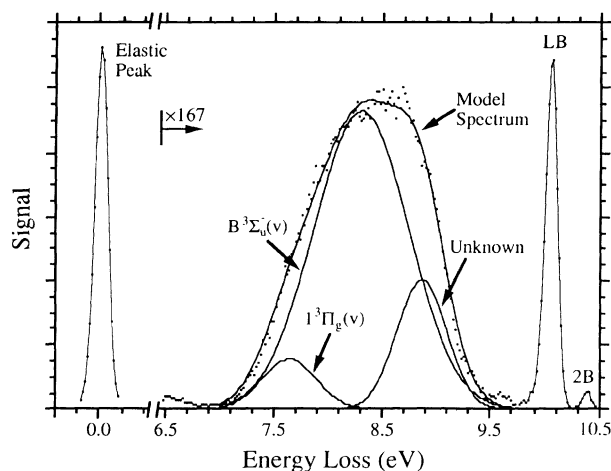


FIG. 1. A typical electron-energy-loss spectrum for the Schumann-Runge continuum of O_2 along with the corresponding least-squares fit. The impact energy was 20 eV, while the scattering angle was 156° . Note the change of scale in the right part of this figure. Dots denote the measured data and solid lines in the best-fit line shapes for individual state contributions and the summed model spectrum.

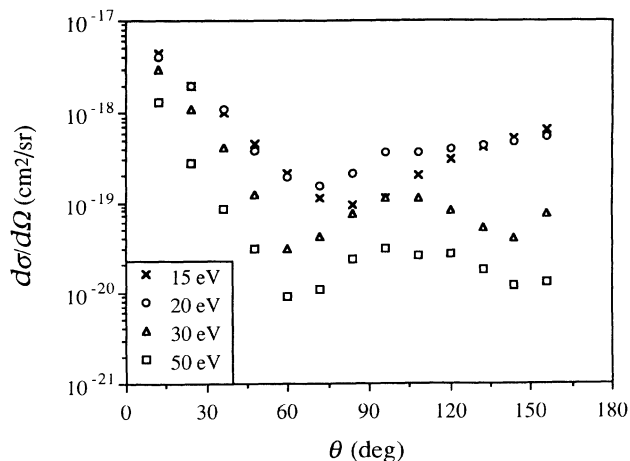


FIG. 2. Differential excitation cross sections for excitation of the $1^3\Pi_g(v)$ state.

IV. DISCUSSION OF RESULTS

Cartwright *et al.* indicated that substantial contributions to the SR continuum were made by four valence states, along with minor contributions from several Rydberg states. Following their lead, we initially employed a four-Gaussian model to describe the spectra. (Recall that we ignored the small Rydberg state contributions to keep the analysis computationally manageable.) The fourth Gaussian consistently proved itself superfluous, so for final analysis we employed only three. All model parameters were allowed to vary independently. The widths and centers of the Gaussians remained constant to within a few percent throughout the analysis, while the intensities of the Gaussians changed. Initial choices for the parameters describing the Gaussians were obtained by consideration of the results of others, especially Lee *et al.* for the $B^3\Sigma_u^-(v)$ state. The two parameters of lowest vertical excitation energy were identified as representing the $1^3\Pi_g(v)$ and $B^3\Sigma_u^-(v)$ states, respectively. The remain-

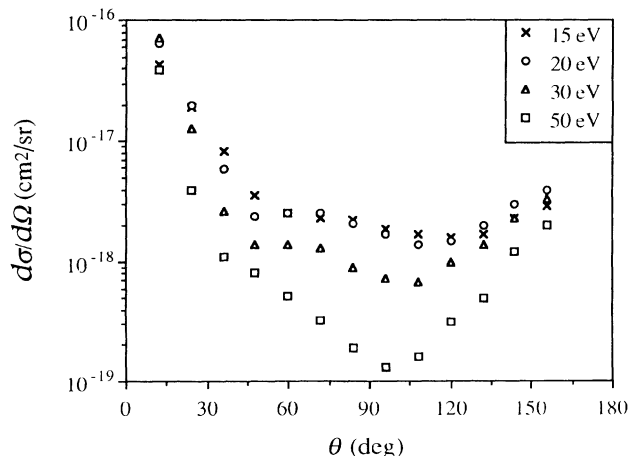


FIG. 3. Differential excitation cross sections for excitation of the $B^3\Sigma_u^-(v)$ state.

TABLE II. Mean excitation energies V_0 , energy widths FWHM, and slopes γ for the states contributing to the SR continuum, as determined by electron-impact experiments.

State	Researchers	V_0 (eV)	FWHM (eV)	γ (eV/Å)
$1^3\Pi_g(v)$	Present	7.65 ± 0.03	0.60 ± 0.08	-6.88 ± 0.87
	Cartwright <i>et al.</i>	7.50 ± 0.10	0.95	-11.1
	Spence	7.6		
$B^3\Sigma_u^-(v)$	Present	8.34 ± 0.02	1.04 ± 0.03	-12.1 ± 0.4
	Cartwright <i>et al.</i>	8.30 ± 0.05	1.19	-13.9
Unknown	Present	8.87 ± 0.02	0.58 ± 0.03	-6.66 ± 0.29

ing Gaussian cannot be definitively identified and may in fact arise from several sources.

Figure 1 shows a typical decomposed energy-loss spectrum at 20-eV impact energy and a scattering angle of 156° . The small bulge on the low-energy side of this spectrum corresponds to excitation of the $1^3\Pi_g(v)$ state. The center Gaussian corresponds to excitation of the $B^3\Sigma_u^-(v)$ state, and excitation of the unknown state is indicated by the Gaussian on the high-energy-loss side. Table II gives the center and energy FWHM of each state along with several previously published values. The slope of the potential-energy curve of each state in the FC region calculated by means of Eq. (5) is also provided in this table.

Table III lists cross sections for excitation of the $1^3\Pi_g(v)$ state by electron impact. Figure 2 illustrates the differential excitation cross sections. The 15-eV results show both strong forward and backward scattering, along with a minimum near 80° . In the 20-eV results, the minimum moves downward in angle to about 70° , and the middle angle scattering becomes stronger. The minimum moves to about 60° in the 30- and 50-eV cross sections. Additionally, the backscattering diminishes at these higher energies.

The cross sections we obtained for excitation of the $B^3\Sigma_u^-(v)$ state are supplied in Table IV. Figure 3 displays the differential excitation cross sections. At all four impact energies, the angular distributions have the same characteristic shape: strong forward scattering, along with two local minima, indicating *D*-wave character. The lower angle minimum is fairly weak and occurs at about 60° for the 15-eV results. As the impact energy increases to 50 eV, this minimum moves downward to about 30° . The higher angle minimum occurs at about

120° for 15-eV impact. As the impact energy increases to 50 eV, it becomes more pronounced and moves downward in angle to about 95° .

In Table V, we list excitation cross sections for the unidentified state. This state may be composite in nature. Figure 4 shows the differential cross sections; the angular distributions bear a curious resemblance to those for the $B^3\Sigma_u^-(v)$ state. The cross sections' magnitudes vary over about three decades with strong forward scattering. Two minima are apparent; the lowest in angle of these occurs at about 50° at 15-eV impact and moves downward slightly as the impact energy increases. The other minimum appears at about 120° at 15-eV impact and moves downward in angle to about 100° as the impact energy increases.

Figure 5 illustrates the integrated cross sections we determined for the three excitations. The $1^3\Pi_g(v)$ and $B^3\Sigma_u^-(v)$ state excitation cross sections exhibit nearly the same character with respect to impact energy, with a maximum at about 20 eV. The $1^3\Pi_g(v)$ -state cross sections have a substantially smaller magnitude than $B^3\Sigma_u^-(v)$ -state cross sections, however, and diminish more rapidly than those of the $B^3\Sigma_u^-(v)$ state as the impact energy increases. The cross sections associated with the unidentified line shape have a magnitude between those of the other two sets of integrated cross sections. For these cross sections, the maximum appears at about 30 eV.

As seen in Table II, the mean vertical excitation energies determined by electron-scattering experiments for the $1^3\Pi_g(v)$ state agree well, but the slopes differ markedly. These differences may reflect the difficulty in isolating the state's excitation peak from the strong background of

TABLE III. Absolute cross sections for the excitation of the $1^3\Pi_g(v)$ state of molecular oxygen by electron impact. Units for the differential cross sections are 10^{-19} cm²/sr, while those for the integrated cross sections are 10^{-18} cm². Parentheses enclose interpolated or extrapolated values.

θ (deg)	12	24	36	48	60	72	84	96	108	120	132	144	156	168	σ_i
E (eV)															
15	44	20	10	4.5	2.1	1.1	0.93	1.1	2.0	3.0	4.2	5.2	6.4	(8.1)	6.5
20	40	20	11	3.8	1.9	1.5	2.1	3.6	3.6	4.0	4.3	4.7	5.4	(6.0)	7.0
30	30	11	4.1	1.2	0.30	0.41	0.75	1.1	1.1	0.81	0.52	0.40	0.74	(0.85)	2.8
50	13	2.8	0.84	0.31	(0.090)	(0.11)	0.23	0.31	0.25	0.26	0.18	(0.12)	(0.13)	(0.14)	0.94

TABLE IV. Absolute cross sections for the excitation of the $B^3\Sigma_u^-$ state of molecular oxygen by electron impact. Units for the differential cross sections are 10^{-18} cm²/sr, while those for the integrated cross sections are 10^{-17} cm². Parentheses enclose extrapolated values.

θ (deg)	12	24	36	48	60	72	84	96	108	120	132	144	156	168	σ_i
E (eV)															
15	43	19	8.2	3.6	2.5	2.3	2.2	1.9	1.7	1.6	1.7	2.3	2.9	(3.3)	5.3
20	64	20	5.8	2.4	2.5	2.5	2.1	1.7	1.4	1.5	2.0	3.0	4.0	(5.5)	5.8
30	71	13	2.6	1.4	1.4	1.3	0.89	0.72	0.68	0.99	1.4	2.3	3.3	(4.3)	4.4
50	39	4.0	1.1	0.80	0.53	0.32	0.19	0.13	0.16	0.31	0.51	1.2	2.0	(3.0)	2.0

the optically allowed $B^3\Sigma_u^-(v)$ component of the SR continuum. While Spence [39] did not tabulate the numerical value he determined for the slope, he did indicate that its slope passes completely under the minimum of the $C^3\Pi_g(R)$ curve. Theoretical predictions indicate that for states of this symmetry in O₂, however, the perturbations are weak. The results of Cartwright *et al.* show that the $1^3\Pi_g(v)$ state's curve crosses the $C^3\Pi_g(R)$ state's curve on its outer limb near its ground vibrational state energy of 8.15 eV, which is consistent with the notion of weak perturbations. Our results permit the possibility of perturbations intermediate in magnitude.

The mean vertical excitation energy and slope of the FC region potential-energy curve we determined for the $B^3\Sigma_u^-(v)$ state agree well with the results of Cartwright *et al.* In addition, our curve joins smoothly with the bound portion of the $B^3\Sigma_u^-(v)$ -state curve deduced from photoabsorption experiments [40].

The potential-energy curve corresponding to the Gaussian highest in mean vertical excitation energy correlates reasonably well with those obtained by Cartwright *et al.* for the $1^3\Pi_u(v)$ state, suggesting that this is in fact the state we have observed. In addition, there is the possibility that it represents an as of yet unidentified state, perhaps the 8.93-eV state posited to exist by Cartwright *et al.* Alternatively, the line shape may be a computational artifact representing some combination of a transition moment decrease in the $B^3\Sigma_u^-(v) \leftarrow X^3\Sigma_g^-(v)$

transition for small internuclear distances and a perturbation to the assumed linear form of the FC region potential-energy curve. This interpretation is supported by the resemblance of the angular distributions for the $B^3\Sigma_u^-(v)$ -state cross sections to those of the unidentified excitation and is also suggested by the theoretical calculations. The configuration-interaction (CI) calculations of Yoshimine *et al.*, for instance, showed strong evidence of perturbations to this potential-energy curve by the nearby $2^3\Sigma_u^-(R)$ potential-energy curve. Their calculations also indicated a nonconstant transition moment. Julienne, Neumann, and Krauss obtained qualitatively similar results from their calculations. The CI calculations of Buenker and Peyerimhoff [8] also indicated strong perturbations between valence and Rydberg states of this symmetry in molecular oxygen, with the $B^3\Sigma_u^-(v)$ state potential-energy curve exhibiting a pronounced falloff for higher excitation energies in the FC region. Similar trends are apparent from the calculations of Saxon and Liu [12].

V. CONCLUSION

We have measured electron-energy-loss spectra for excitation of the Schumann-Runge continuum of molecular oxygen. The scattering angle and impact-energy ranges covered were 12°–156° and 15–50 eV, respectively. The spectra were decomposed into three principal Gaussian

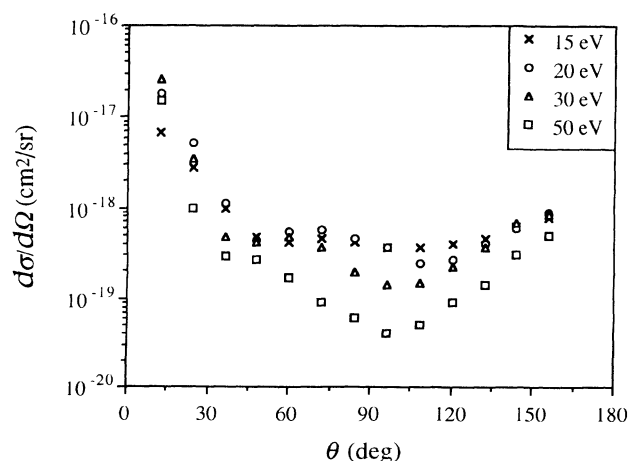


FIG. 4. Differential excitation cross sections for the unidentified excitation.

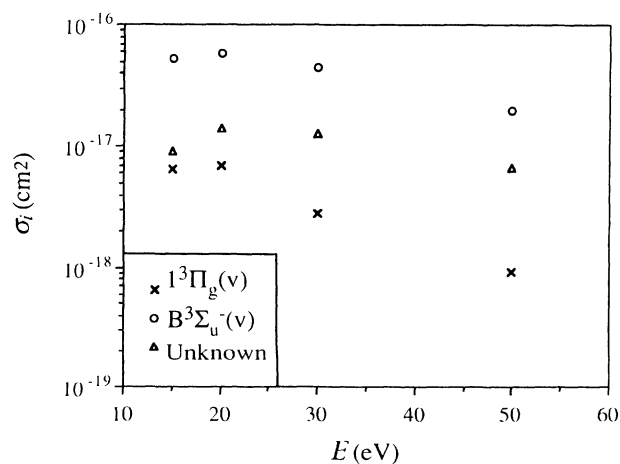


FIG. 5. Integrated cross sections for the excitation of the $1^3\Pi_g(v)$ and $B^3\Sigma_u^-(v)$ states of O₂ along with those for the unidentified excitation.

TABLE V. Absolute cross sections for the excitation of the unknown state of molecular oxygen by electron impact. Units for the differential cross sections are 10^{-18} cm²/sr, while those for the integrated cross sections are 10^{-17} cm². Parentheses enclose extrapolated values.

E (eV) \ θ (deg)	12	24	36	48	60	72	84	96	108	120	132	144	156	168	σ_i
15	6.6	2.7	1.0	0.48	0.42	0.45	0.41	0.37	0.37	0.39	0.45	0.62	0.78	(0.9)	0.92
20	18	5.2	1.1	0.44	0.55	0.57	0.45	0.36	0.24	0.26	0.40	0.61	0.90	(1.5)	1.4
30	26	3.4	0.48	0.41	0.48	0.37	0.19	0.14	0.15	0.22	0.37	0.67	0.85	(1.0)	1.3
50	15	1.0	0.29	0.27	0.17	0.09	0.06	0.04	0.05	0.09	0.14	0.31	0.49	(0.8)	0.67

contributions by extensive computerized least-squares analysis, and absolute excitation cross sections for each contribution were obtained along with FC region potential-energy curves. The results may be of particular importance to atmospheric scientists, as excitation of the SR band of molecular oxygen is not only important in determining atmospheric transmission in the ultraviolet but is also a source of oxygen atoms in their ground 3P and excited 1D states. Two of the three principal contributions were identified as arising from the transitions $1^3\Pi_g(v) \leftarrow X^3\Sigma_g^-$ and $B^3\Sigma_u^-(v) \leftarrow X^3\Sigma_g^-$. The third contribution has not been definitively identified and may arise from several sources, as we have indicated. Our approach was limited by the assumptions of constant transition moments and linear FC region potential-energy curves. Further progress in decomposing SR spectra will

rely on the accurate calculation of corrections to these assumptions.

ACKNOWLEDGMENTS

The authors gratefully acknowledge support for this research provided by National Science Foundation Grant Nos. ATM-8913022 and ATM-9205041. Computational support provided by the Pittsburgh Supercomputing Center under Grant No. PHY920020P and also by the Computer Aided Engineering Network (CAEN) at the University of Michigan is greatly appreciated. Dr. David C. Cartwright is gratefully acknowledged for participating with the authors in private conversations that provided valuable insight into the nature of the Schumann-Runge continuum of molecular oxygen.

- [1] M. Nicolet and W. Peetermans, *Planet. Space Sci.* **28**, 85 (1980).
- [2] M. Allen and J. E. Fredrick, *J. Atmos. Sci.* **39**, 2066 (1982).
- [3] R. Ladenburg and C. C. Van Voorhis, *Phys. Rev.* **43**, 315 (1933).
- [4] R. D. Hudson, *Rev. Geophys. Space Phys.* **9**, 305 (1972).
- [5] P. H. Krupenie, *J. Phys. Chem. Ref. Data* **1**, 423 (1972).
- [6] L. C. Lee, T. G. Slinger, G. Black, and R. L. Sharpless, *J. Chem. Phys.* **67**, 5602 (1977).
- [7] R. J. Buenker, S. D. Peyerimhoff, and M. Peri, *Chem. Phys. Lett.* **42**, 383 (1976).
- [8] R. J. Buenker and S. D. Peyerimhoff, *Chem. Phys. Lett.* **34**, 225 (1975).
- [9] P. S. Julienne, D. Neumann, and M. Krauss, *J. Chem. Phys.* **64**, 2990 (1976).
- [10] R. P. Saxon and B. Liu, *J. Chem. Phys.* **67**, 5432 (1977).
- [11] R. P. Saxon and B. Liu, *J. Chem. Phys.* **73**, 870 (1980).
- [12] R. P. Saxon and B. Liu, *J. Chem. Phys.* **73**, 876 (1980).
- [13] M. Yoshimine, H. Tatewaki, S. Obara, F. Sasaki, and K. Ohno, *J. Chem. Phys.* **64**, 2254 (1976).
- [14] S. Trajmar, D. F. Register, and A. Chutjian, *Phys. Rep.* **97**, 219 (1983).
- [15] S. Trajmar and D. C. Cartwright, *Electron Molecule Interactions and Their Applications*, edited by L. G. Christophorou (Academic, New York, 1984), Vol. 1, Chap. II, pp. 154–250.
- [16] Y. Itikawa, A. Ichimura, K. Onda, K. Sakimoto, K. Takayanagi, Y. Hatano, M. Hayashi, H. Nishimura, and S. Tsurubuchi, *J. Phys. Chem. Ref. Data* **18**, 23 (1989).
- [17] K. Wakiya, *J. Phys. B* **11**, 3913 (1978).
- [18] K. Wakiya, *J. Phys. B* **11**, 3931 (1978).
- [19] S. Trajmar, D. C. Cartwright, and R. I. Hall, *J. Chem. Phys.* **65**, 5275 (1976).
- [20] T. A. York, and J. Comer, *J. Phys. B* **16**, 3627 (1983).
- [21] A. Sur, C. V. Ramana, and S. D. Colson, *J. Chem. Phys.* **83**, 904 (1985).
- [22] A. Sur, C. V. Ramana, W. A. Chupka, and S. D. Colson, *J. Chem. Phys.* **84**, 69 (1986).
- [23] D. C. Cartwright, N. A. Fiamengo, W. Williams, and S. Trajmar, *J. Phys. B* **9**, L419 (1976).
- [24] J. Geiger and B. Schröder, *J. Chem. Phys.* **49**, 740 (1968).
- [25] T. W. Shyn and W. E. Sharp, *Phys. Rev. A* **26**, 1369 (1982).
- [26] T. W. Shyn and W. E. Sharp, *Phys. Rev. A* **43**, 2300 (1991).
- [27] T. W. Shyn and C. J. Sweeney, *Phys. Rev. A* **47**, 1006 (1993).
- [28] T. W. Shyn and C. J. Sweeney, *Phys. Rev. A* **48**, 1214 (1993).
- [29] T. W. Shyn, C. J. Sweeney, and A. Grafe, *Phys. Rev. A* **49**, 3680 (1994).
- [30] T. W. Shyn, R.S. Stolarski, and G. R. Carignan, *Phys. Rev. A* **6**, 1002 (1972).
- [31] T. W. Shyn and A. Grafe, *Phys. Rev. A* **46**, 4406 (1992).
- [32] T. W. Shyn and C. J. Sweeney, *Phys. Rev. A* **47**, 2919 (1993).
- [33] W. H. Press, S. A. Teukolsky, W. T. Vetterling, and B. P.

- Flannery, *Numerical Recipes*, 2nd ed. (Cambridge University Press, Cambridge, England, 1992).
- [34] W. L. Morgan, *IEEE Trans. Plasma Sci.* **19**, 250 (1991).
- [35] W. H. Press and S. A. Teukolsky, *Comput. Phys.* **5**, 426 (1991).
- [36] J. Franck, *Trans. Faraday Soc.* **21**, 536 (1925).
- [37] E. U. Condon, *Phys. Rev.* **28**, 1182 (1926).
- [38] E. U. Condon, *Phys. Rev.* **32**, 858 (1928).
- [39] D. Spence, *J. Chem. Phys.* **74**, 3889 (1981).
- [40] D. L. Albritton, A. L. Schmeltekopf, and R. N. Zare, *Diatom Intensity Factors* (Harper and Row, New York, 1976).